African Journal of Geophysics and Earth Sciences (AJGES)
E-ISSN 2978- 3305 (Online); ISSN 2978- 3291 (Print)

Indexed by SABINET, ProQuest and EBSCO

Volume 2, Number 1, June 2026

Pp 47-64

Integration of ASTER Multispectral Data and Spectral Angle Mapper Classification for the Mapping of New Hydrothermal Alteration Zones (Tiouit, Eastern Anti-Atlas, Morocco)

DOI: https://doi.org/10.31920/2978-3305/2026/v2n1a3

Abdelhalim Miftah
Hassan First University of Settat, Faculty of Sciences and Technology, Laboratory Physico-Chemistry of Processes and Materials, Research Team Geology of the Mining and Energetics Resources, Settat, Morocco.
E-mail: a.miftah@uhp.ac.ma

Abstract

In this paper, the problem of hydrothermal alteration mapping in the Tiouit gold district has been investigated using ASTER multispectral data and the supervised Spectral Angle Mapper (SAM) classification technique. Following the image preprocessing steps, the spectral signatures of the main mineralogical phases of interest have been extracted and analyzed to identify and discriminate the different alteration facies. By employing an optimal angular threshold, an accurate and consistent alteration map has been produced. The results of the analysis have shown that the main hydrothermal alteration facies present in the region under investigation are propylitic, argillic, phyllic, and ferruginous. In the central, eastern, and southern parts of the region, ferruginous alteration dominates, while chloritization tends to be more developed in the North and in the footwall of the mineralized structures. In the intermediate position, argillic and phyllic alterations have been observed, indicating a well-structured hydrothermal zoning pattern. Spatial analysis of the results has shown a strrong correlation between the alteration zoning and the structural network of the region, which confirms the important role of tectonics in controlling the direction of the hydrothermal fluids. In conclusion, the results of the analysis have validated the effectiveness of multispectral remote sensing as a useful tool for the identification of prospective areas in arid mining environments.

Keywords: *Hydrothermal alteration, ASTER, Spectral Angle Mapper, Multispectral remote sensing, Tiouit gold district, Eastern Anti-Atlas.*

Introduction

The identification of hydrothermal alteration zones is considered a basic step in mineral exploration. Ore deposits are commonly formed through hydrothermal fluid circulation that modifies the mineralogy and geochemistry of the host rocks. Numerous previous studies have demonstrated the reliability of multispectral data analysis for detecting alteration zones. These approaches provide rapid and effective information on the physicochemical variations associated with hydrothermal fluids at the surface (Bedini, 2011; Kruse et al., 2003; Miftah et al., 2022).

Supergene alteration processes generate an oxidized zone characterized by abundant iron oxides and/or hydroxides (yellowish to reddish altered rocks), collectively referred to as gossans (Abdelsalam and Stern, 2000; Miftah et al., 2022; Sabins, 1999). Among these minerals, limonite, jarosite, and hematite are commonly observed. They typically exhibit low reflectance in the visible range and higher reflectance in the near-infrared region of the electromagnetic spectrum. Electronic processes produce diagnostic absorption features in the visible and near-infrared (0.4–1.1 μm) due to the presence of transition elements such as Fe^{2+} and Fe^{3+}, which are often substituted by Mn, Cr, and Ni within the crystal structure of minerals (Hunt, 1977; Hunt and Ashley, 1979).

Hydroxyl-bearing minerals, including clay and sulfate groups, as well as carbonate minerals, exhibit distinct spectral characteristics resulting from fundamental vibrational absorption processes of Al–O–H, Mg–O–H, Si–O–H, and CO_3 groups in the infrared domain. Consequently, infrared data acquired by multispectral sensors can be used to identify hydrothermal alteration mineral assemblages, including: (i) mineralogy generated by the circulation of low-pH fluids (e.g., alunite and pyrophyllite); (ii) Al–Si–OH and Mg–Si–OH–bearing minerals, including kaolinite, mica, and chlorite groups; and (iii) Ca–Al–Si–OH–bearing minerals such as the epidote group, as well as carbonate minerals

(Beiranvand Pour and Hashim, 2012, 2014; Clark et al., 1990; Hunt, 1977; Huntington, 2007).

The selection of the ASTER sensor is based on itsj adequate spectral resolution in the shortwave infrared (SWIR) bands, which is particularly suitable for mapping mineralized zones associated with hydrothermal mineralization. These zones can be effectively detected and delineated using multispectral remote sensing techniques because they typically span areas much larger than the spatial resolution of the available multispectral data. Based on the spectral properties of the mineral background and the alteration types, the Spectral Angle Mapper (SAM) classification method was applied to map hydrothermal alteration zonation (De Carvalho and Meneses, 2000; Hunter and Power, 2002; Kruse et al., 1993; Schwarz and Staenz, 2001; Van der Meer et al., 1997).

Geological Context:

The granodioritic body carrying the Tiouit gold mineralization makes up a fundamental part of the plutonic complex of the Late Proterozoic period. This makes up a significant part of the Jbel Saghro massif, which is a part of the Anti-Atlas mountain range that is known for its significant mineral wealth, located along the Northern edge of the West African Craton (Figure 1).

The Anti-Atlas extends over an area of approximately 700 × 200 km, trending WSW–ENE from the Atlantic coast in the West to the Tafilalt region in the East. It is bounded to the North by the South Atlas Fault, which marks a major discontinuity between the Saharan metacratonic domain to the South and the Meseta–Atlas domain with Hercynian basement to the North. The Anti-Atlas belt extends from the Atlantic margin near Agadir toward Eastern Morocco (Gasquet, 1991). Its Southeastern boundary is delineated by the Carboniferous Tindouf Basin, associated with the belt of extensive Tertiary and Mesozoic Hamadas of the Draa, Guir, and Kem Kem regions (Choubert and Faure-Muret, 1980; Hefferan et al., 1992; Leblanc and Lancelot, 1980).

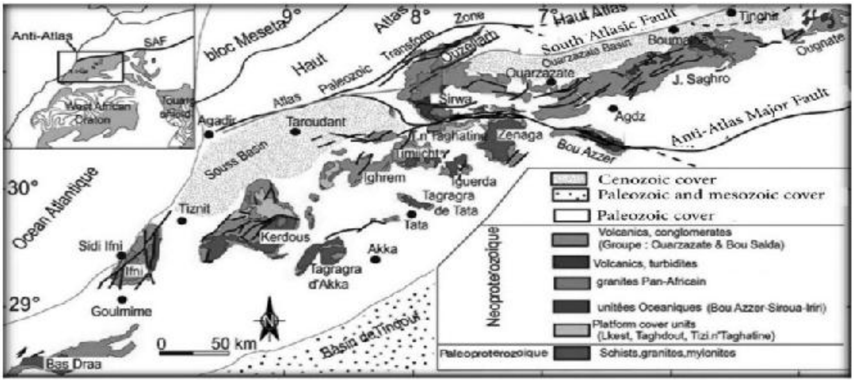

Figure 1: Geological map of the Anti-Atlas. (Gasquet et al., 2008).

Lithological Units of the Tiouit Mining Area:

Volcano-Sedimentary Series:

To the North and Northeast of Tiouit (Figure 2), a Lower PII schistose formation cropped out, characterized by an alteration of grey quartz-feldspathic sandstones and grey to purplish pelites. The prevailing folding direction is given as N-S to N10°E (El Hjouji, 1990). Benziane (1990) considers that the mentioned sandstones are a part of a flysch series that essentially comprises volcanic rocks.

All these formations underwent low-temperature metamorphism of the epizonal type during the principal tectonic period of the Pan-African orogeny. This interpretation is supported by the presence of minerals like chlorite, epidote, sericite, actinolite, and albite (Argollo et al., 1982; Benkirane, 1987; Saquaque, 1992). In the same studies, the development of a higher level of metamorphism in the direction of the Tiouit - Iknioun pluton was observed, as supported by the presence of biotite, cordierite, andalusite, garnet, muscovite and/or paragonite, and green hornblende. The volcano-sedimentary series was intruded by rhyolite, aplite, trachyte, and dolerite dykes (Benkirane, 1987).

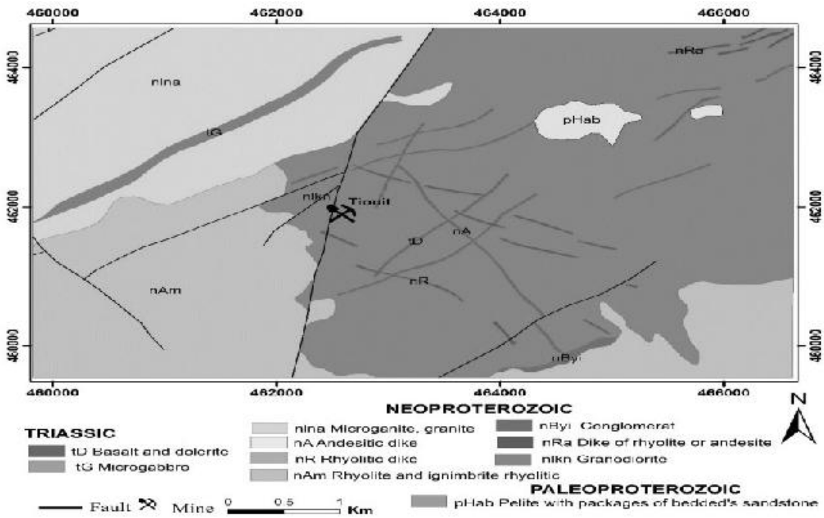

Figure 2 : Geological map of the study area (Hawkins et al., 2001).

Magmatic Units:

-Lower PII Granitoids of Tiouit: This formation comprises a large massif with an irregular border (Figure 2). Ameur (1986) described three major facies in the Lower PII Granitoids of Tiouit as follows:

- Calc-alkaline granites: This facies of the Lower PII Granitoids of Tiouit occurs in the SW of the region. It features subhorizontal slab-like fracturing with thicknesses of a few meters. It has a holocrystalline texture and a subautomorphic granular texture (Jettane, 1995).
- Monzonitic trending granodiorite: The Tiouit Granodiorite is a very large and highly tectonized massif of variable size. It features a granular texture with a grain size of 3 to 6 mm. The presence of andalusite in the chloritized facies in the North results from contact metamorphism of the Lower PII Granodiorite and the Upper PII Granophyre (Mathieux et al., 1982).

-Rhyo-Ignimbritic Flows (Figure 2): Rhyo-ignimbritic flows are accumulations of acidic lava debris, which are dominated by rhyolites and rhyodacites. They occur North-South across the Tiouit pluton and unconformably cover the southern part of the pluton (Chaker, 1997). They cover an area of about 25 km² and have a striking direction of N130° to

N100° (Benkirane, 1987). They form part of the Upper PII Volcanic and Pyroclastic assemblage (Saquaque, 1992).

-Lower PII Alkaline Granites: The Isk-n-Alla Granite, which has an age of 558 ± 5 Ma, intrudes the western part of the Tiouit pluton (Figure 2). This type of granite extends in a NE-SW direction for about 46 km and has a width of about 10 km. It is bounded by the two Tagmout faults, forming a horst structure (Benchekroun, 2007). It features dominant pink facies and red facies common in the margins of the intrusion.

-Dykes: Both Lower and Upper PII formations are traversed by late-stage dykes of varying densities in different areas (Figure 2). By composition, these range from acidic to intermediate types and include rhyolite, andesite, and trachyandesite. They intersect the Tiouit pluton in two main preferred orientations of NW–SE and SW–NE (Benkirane, 1987; Combe and Morrelli, 1983; El Maghraoui and Popov, 1982). Ameur (1986) states that each of these sets of dykes shows a preferred orientation with dips generally vertical but slightly inclined in the NE direction.

Rhyolite dykes are colored from light to pink and are more common in the NW–SE direction. Together with microgranite dykes, these represent eruptive phases in the Upper PII. Trachyandesite and porphyritic andesite are more likely to have crossed rhyolite and microgranite dykes and are therefore of later age and represent the final manifestations of the Upper PII (Jettane, 1995). Dolerite and microgabbro are of Hercynian age and are NE–SW trending, just like trachyandesite and porphyritic andesite (Combe and Morrelli, 1983).

2.2. Structural Control of Gold Mineralization in the Tiouit Pluton:

The dip of the joints in the Tiouit pluton occurs at a shallow angle and in a subhorizontal direction, gently inclining towards the SE at angles ranging from 10° to 30° (Figure 2). The gold deposits are concentrated in the joints, and the joints are likely related to the cooling and subsequent contraction of the pluton (Argollo et al., 1982; El Maghraoui and Popov, 1982). The joints are sometimes accompanied by tension fractures, causing negligible deformation in the rocks. The rocks are also characterized by fractures of different orientations, including N030, N110, and N-S (Chaker, 1997).

The Northwestern and Western areas of the Tiouit pluton, where the gold deposits are found, are characterized by a series of dykes and fault systems. The structural setting suggests that the permeability of the rocks in the area is enhanced, facilitating the movement of fluids. The fault families affecting the Tiouit pluton are broadly similar to those recognized in the currently exploited zones of the gold deposit hosted within the pluton (Argollo et al., 1982).

Materials and Methods:

ASTER Image Preprocessing:

Since 2000, the Advanced Spaceborne Thermal Emission and Reflection Radiometer (ASTER) has been successfully used for hydrothermal alteration mineral mapping in well-exposed outcrop areas (Aboelkhair et al., 2010; Beiranvand Pour and Hashim, 2014; Crósta et al., 2003; Gabr et al., 2015; Hassan and Sadek, 2017; Zoheir and Emam, 2014).

ASTER is a highly advanced multispectral imaging system launched aboard the Terra spacecraft in December 1999 by NASA and METI (Japan Ministry of Economy, Trade and Industry). It measures reflected radiation in the visible and near-infrared (VNIR) region (0.52–0.86 μm), shortwave infrared (SWIR) region (1.16–2.43 μm), and emitted thermal infrared (TIR) radiation (8.125–11.65 μm), with 3, 6, and 5 spectral bands, respectively, and spatial resolutions of 15 m, 30 m, and 90 m. The swath width of ASTER is 60 km, while its pointing capability extends the total observation coverage up to 232 km (Abrams et al., 2002; Sabins, 1999) (Table 1).

Table 1. Characteristics of the ASTER Sensor (Abrams et al., 2002).

Spectral Region	VNIR	SWIR	TIR
Spectral Range (µm)	1: 0.52 - 0.60 2: 0.63 - 0.69 3N: 0.78 - 0.86 3B: 0.78 - 0.86	4: 1.650 - 1.700 5: 2.145 - 2.185 6: 2.185 - 2.225 7: 2.235 - 2.285 8: 2.295 - 2.395 9: 2.360 - 2.430	10: 8.125 - 8.475 11: 8.475 - 8.825 12: 8.925 - 9.275 13: 10.25 - 10.95 14: 10.95 - 11.65
Spatial resolution (m)	15	30	90
Data rate (Mbits/s)	62	23	4.2
Cross-track pointing (°)	±24	±8.55	±8.55
Cross-track pointing (km)	±318	±116	±116
Swath width (km)	60	60	60
Detector type	Si	PtSi-Si	HgCdTe
Quantization (bits)	8	8	12

The Level 1B ASTER image (sensor radiance), acquired on September 9, 2000, with 0% cloud cover, was radiometrically calibrated and geometrically corrected. All bands were atmospherically corrected using the Fast Line-of-sight Atmospheric Analysis of Spectral Hypercubes (FLAASH) module (Bedini, 2011; Beiranvand Pour and Hashim, 2014). Subsequently, a subset of the full scene covering only the study area was extracted and reprojected from the Universal Transverse Mercator (UTM) coordinate system (WGS84 datum, Zone 30N) to the Lambert Conformal Conic Zone II projection system to ensure compatibility with the available geological data.

Spectral Angle Mapper (SAM) Classification:

The SAM technique, developed by Kruse et al. (1993), is a supervised image classification technique that facilitates rapid mapping through the evaluation of spectral similarity between image spectra and reference reflectance spectra. The spectrum may be obtained through either image extraction or through field/laboratory measurements (De Carvalho and Meneses, 2000; Hunter and Power, 2002; Kruse et al., 1993; Miftah et al., 2022; Rowan and Mars, 2003; Schwarz and Staenz, 2001; Van der Meer et al., 1997; Yuhas et al., 1992).

In an n-band multispectral image, each pixel can be considered as a vector in an n-dimensional feature space X (Figure 3). The vector magnitude (length) is determined by the numerical pixel values across all bands, while the vector direction is defined by the shape of the pixel's spectral profile. If two pixels exhibit similar spectral properties but are illuminated differently due to topographic effects, their corresponding vectors will have different magnitudes but very similar directions. Therefore, pixel classification based on spectral angle measurements is independent of topographic illumination effects as well as any unknown linear translation factors (Kruse et al., 1993; Liu and Mason, 2016).

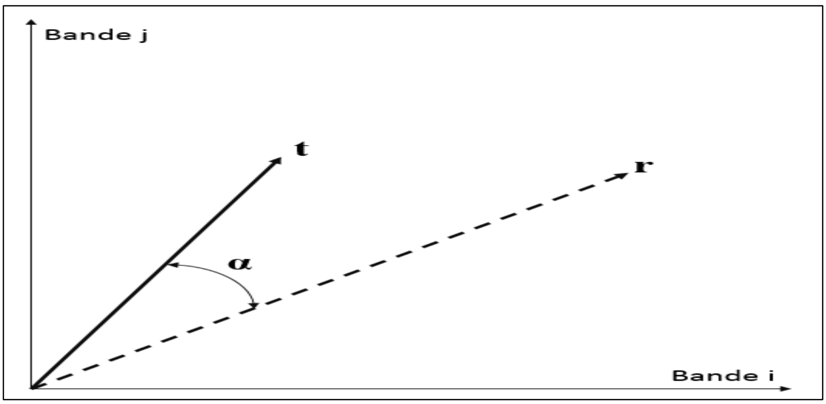

Figure 3: Graphical illustration of two spectral vectors and the spectral angle (a). r: reference spectral vector; t: image spectral vector.

The algorithm that determines the similarity between two spectra by calculating the spectral angle between them is illustrated in the two-dimensional representation (Figure 3). According to vector algebra, the angle (α) between the two vectors **r** and **t** is defined by Equation:

$$\alpha = \cos^{-1}\left(\frac{t.r}{|t|.|r|}\right) = \cos^{-1}\left[\frac{\sum_{i=1}^{m} t_i r_i}{\left(\sum_{i=1}^{m} t_i^2\right)^{1/2}\left(\sum_{i=1}^{m} r_i^2\right)^{1/2}}\right] \quad \text{(Eq.1)}$$

where *m* represents the number of spectral bands.

The spectral signatures of specific minerals that are present in every alteration type were selected based on their reflectance differences to avoid any spectral overlap that may cause redundancy or confusion. Finally, chlorite, alunite, illite, and hematite were selected to represent propylitic, argillic, phyllic, and ferruginous alterations, respectively, based on their significant differences in spectral characteristics (Figure 4a). These spectral signatures were resampled using a high-pass filter to match the spectral bands of the ASTER image, whose wavelengths range from 0.3 to 2.5 μm (Figure 4b).

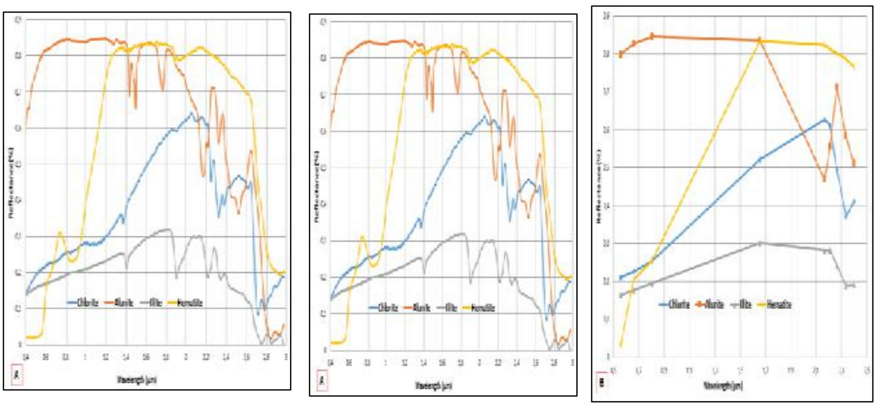

Figure 4:a) Spectral signatures of minerals associated with different hydrothermal alterations. Chlorite, alunite, illite, and hematite are associated with propylitic, argillic, phyllic, and iron oxide alterations, res pectively (Clark et al., 1993). b) Resampled spectral signatures using a high pass filter for corresponden ce with the spectral bands of the ASTER image, covering 0.3–2.5 μm.

Results and Discussion:

The use of Spectral Angle Mapper classification for ASTER data allowed for rapid and efficient identification of the spectral similarity between image pixel data and reference data for minerals associated with hydrothermal alterations. This method, based on the computation of the spectral angle (α), provides its major advantage in reducing effects of illumination changes and shadowing due to topography, thereby emphasizing inherent spectral properties of minerals.

The pixel data were converted from radiance units to reflectance units for use in the Spectral Angle Mapper algorithm. This ensured that all data were consistent for use in the algorithm. The angle used in the algorithm was set at 3 degrees; this value allowed for optimal discrimination between different hydrothermal alteration types and for accurate identification of hydrothermal alteration areas.

The hydrothermal alteration distribution maps (Figure 5) show the major hydrothermal alteration areas in the region, with special emphasis on the Tiouit gold mining region. This region shows marked hematitization with associated chloritization of the Iknioun granodiorite. Spatial distribution of hydrothermal alterations is consistent with the presence of a hydrothermal halo consistent with a porphyry copper deposit of epithermal character, as proposed in earlier metallogenic models (Alansari, 1997; Chaker, 1997).

The structural study indicates a close relationship between areas of significant alteration and the regional network of tectonic fractures. The faults with a N-S to NNE-SSE trend show displacements of up to 50 m and are associated with areas of significant brecciation, which correspond to late structural settings filled by quartz and barite veining (Alansari, 1997; Chaker, 1997; Jettane, 1995). The NW-SE and NE-SW fault systems, which are the most developed and structurally conspicuous, correspond to cataclastic shear zones developed under a compressive regime. These shear structures cut through the mineralized bodies and pass through the rhyolitic, porphyritic andesitic, and dacitic dykes, where the contact between the dykes and the country rocks is highly fractured and hematitized (Alansari, 1997; Bouabdellah et al., 2016; Chaker, 1997; Jettane, 1995).

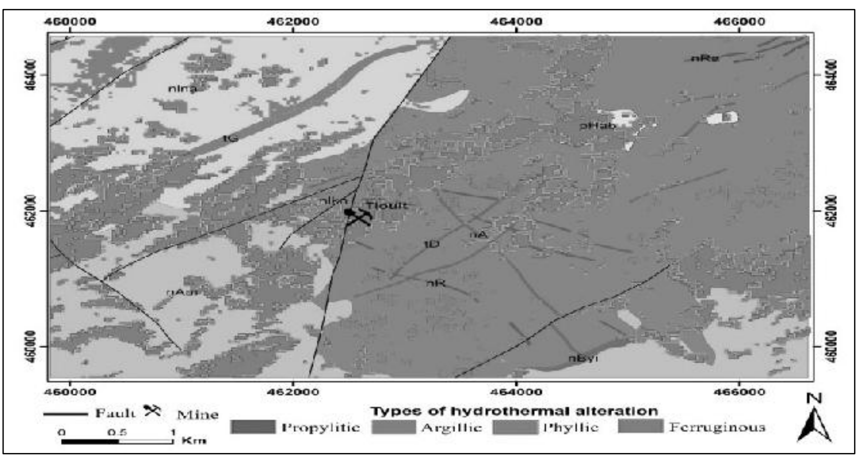

Figure 5 shows the distribution of hydrothermal alteration zones based on the SAM classification results

The subhorizontal faults, dipping gently towards the SE between 10 and 20°, correspond to the oldest structural features. These structures, located on the roof of the Lower PII granodiorite, controlled the emplacement of gold-bearing veins. The brecciated textures of the gold-bearing veins point to syn-mineralization activity, while striations, breccias, and clay-rich alteration zones on the fault walls point to post-mineral reactivation (Alansari, 1997; Bouabdellah et al., 2016; Chaker, 1997; Jettane, 1995).

From a petrographic point of view, the Lower PII granodiorite has experienced different types of hydrothermal alteration, resulting from long exposure to post-magmatic fluids. The dominant alteration types are hematitization and chloritization, with secondary silicification, propylitization, and kaolinization (Alansari, 1997; Bouabdellah et al., 2016; Chaker, 1997)

Hematitization is common throughout the granodioritic massif and takes the form of reddish pigmentation resulting from the partial or total replacement of ferromagnesian minerals by hematite. This phenomenon has developed particularly strongly within the immediate host rocks surrounding the mineralized structures, especially within the southern sector. Here, it has been accompanied by strong silicification phenomena (Alansari, 1997; Chaker, 1997).

In contrast, chloritization has been less widespread and has been observed mainly within the Northern sector and within the footwall of the mineralized structures (Alansari, 1997; Bouabdellah et al., 2016; Chaker, 1997). This phenomenon has been interpreted as an expression of propylitic alteration related to the emplacement of granophyres. An intermediate zone separates the chloritized zone from the hematitized zone and is characterized by equal proportions of chlorite and hematite. This zone can be found between the chloritized Northern zone and the hematitized central, eastern, and southern zones and results from the superimposition of several alteration phenomena. It has also been associated with silicification, sericitization, and argillization phenomena within the mineralized gangue veins (Alansari, 1997; Bouabdellah et al., 2016; Chaker, 1997).

The results have shown that SAM classification can be an effective tool for hydrothermal alteration zone identification and delineation. The results have also shown a strong link between tectonic structures such as faults and dykes and alteration phenomena. It has been concluded that

SAM classification can be highly appropriate for hydrothermal alteration mapping. This method takes into consideration the specific characteristics of each mineral and evaluates the level of similarity with all the spectral variations present within the image. This results in a more precise and restricted delineation of hydrothermal alteration zones.

Conclusion:

The integration of ASTER data and supervised Spectral Angle Mapper (SAM) classification was instrumental in the reliable and spatially consistent mapping of hydrothermal alteration zonation within the Tiouit gold district. The robustness of the spectral signatures used in the analysis was ensured by effective data preprocessing, including reflectance conversion and atmospheric correction.

An angular threshold of 3° was identified as optimal for the differentiation of the major alteration types. The maps obtained from the analysis clearly show the zonation of the different alteration domains, including propylitic, argillic, phyllic, and ferruginous alteration domains. The approach adopted in the study confirms the applicability of multispectral remote sensing in the search for valuable minerals, especially in well-exposed arid regions.

The study reveals a strong structural control of the alteration halos by the fault and dyke systems associated with the Tiouit pluton. The most significant alteration domains are concentrated around the major tectonic axes, suggesting a structural control on hydrothermal fluids. The area where hematitization dominates is the central, eastern, and southern regions, while chloritization is more pronounced in the Northern region and the footwall of the mineralized structures. The existence of a transitional zone also confirms the superposition of hydrothermal phenomena, as expected in the zonal alteration associated with porphyry deposits and epithermal affinities.

The study confirms the applicability of SAM classification in the accurate detection and delineation of hydrothermal alteration zones at the regional scale. The approach adopted in the study can be used as a decision-support tool in mineral exploration, including the optimization of the search process in the field. The study also confirms the metallogenic models proposed for the Tiouit deposit (Alansari, 1997; Bouabdellah et al., 2016; Chaker, 1997; Jettane, 1995; Miftah et al., 2022). The fusion of spectral and structural analysis provides further insight into the behavior of hydrothermal systems, and the applicability of the approach adopted in the study confirms the strategic use of remote sensing as a complement to conventional geological and geochemical investigations.

Acknowledgements:

The authors thank the reviewers for their helpful comments and recommendations.

Declaration of Competing Interest

The authors declare that they have no known competing financial interests or personal relationships that could have appeared to influence the work reported in this paper.

References:

Abdelsalam, M., Stern, R. (2000). Mapping gossans in arid regions with Landsat TM and SIR-C images, the Beddaho Alteration Zone in northern Eritrea. Journal of African Earth Sciences, 30, 903–916.

Aboelkhair, H., Ninomiya, Y., Watanabe, Y., Sato, I. (2010). Processing and interpretation of ASTER TIR data for mapping of rare-metal-enriched albite granitoids in the Central Eastern Desert of Egypt. Journal of African Earth Sciences, 58, 141–151.

Abrams, M., Hook, S., Ramachandran, B. (2002). ASTER user handbook, version 2.

Alansari, A. (1997). La mine d'or de Tiouit: Un exemple de veines aurifères mésothermales, associées à une granodiorite d'âge protérozoïque supérieur (Massif panafricain du Jbel Saghro, Anti-Atlas, Maroc) [Thèse d'Etat ès-sciences]. Faculté Sciences Semlalia, Marrakech.

Ameur, A. (1986). Le district aurifère de Tiouit. Géologie et bilan des travaux. BRPM.

Argollo, J., Loredo-Pérez, J., Matheus, P. (1982). Étude minéralogique et pétrographique de la mine de Tiouit (Maroc) (p. 60). Section d'étude géologique et minière, option géologie minière-ENSUP, Paris.

Bedini, E. (2011). Mineral mapping in the Kap Simpson complex, central East Greenland, using HyMap and ASTER remote sensing data. Advances in Space Research, 47(1), 60–73.

Beiranvand Pour, A., Hashim, M. (2012). The application of ASTER remote sensing data to porphyry copper and epithermal gold deposits . Ore Geology Reviews, 44, 1_9. https://doi.org/10.1016/j.oregeorev.2011.09.009

Beiranvand Pour, A., Hashim, M. (2014). ASTER, ALI and Hyperion sensors data for lithological mapping and ore minerals exploration. Springer Plus, 3, 1–19.

Benchekroun, F. (2007). Modèles minéralogiques et chimiques de dépôt de l'or dans les gisements mésothermaux: Cas de Salsigne (Montagne Noire, France) et de Tiouit (Anti-Atlas, Maroc) [Thèse Doct. Etat]. Univ. Chaïb Doukkali, El Jadida.

Benkirane, Y. (1987). Les minéralisations à W (Sn, Mo, Au, Bi, Ag, Cu, Pb, Zn) du granite de Taourirt-Tamellalt dans leur cadre géologique. La boutonnière protérozoïque du S-E de Boumalne-n-Dades (Saghro oriental, Anti-Atlas, Maroc) [Thèse d'université]. Paris 6.

Benziane, F. (1990). Le Maroc promontoire africain entre la Méditerranée et l'Atlantique.

Bouabdellah, M., Chekroun, F., Alansari, A., Margoum, D. (2016). The granitoid-related Tiouit gold deposit, Saghro inlier, eastern Anti-Atlas (Morocco): Neoproterozoic mineralization by a polyphase late-magmatic to hydrothermal system. In Mineral Deposits of North Africa (pp. 405–414). Springer.

Chaker, M. (1997). Géochimie et métallogénie de la mine d'or de Tiouit, Anti-Atlas oriental (Sud du Maroc) [PhD Thesis]. Université de Chicoutimi, Canada.

Choubert, G., Faure-Muret, A. (1980). L'Anti-Atlas (Morocco). Earth-Science Reviews, 16, 87–113.

Clark, R. N., King, T. V. V., Klejwa, M., Swayze, G. A. (1990). High spectral resolution reflectance spectroscopy of minerals. Journal of Geophysical Research: Solid Earth, 95(B8), 12653–12680.

Clark, R. N., Swayze, G. A., Gallagher, A., King, T. V. V., Calvin, W. M. (1993). The U.S. Geological Survey, Digital Spectral Library: Version 1: 0.2 to 3.0 microns.

Combe, M., Morrelli, S. (1983). Étude de la paragénèse aurifère de la mine de Tiouit (Jbel Saghro, Maroc).

Crósta, A. P., De Souza Filho, C. R., Azevedo, F., Brodie, C. (2003). Targeting key alteration minerals in epithermal deposits in Patagonia, Argentina, using ASTER imagery and principal component analysis. International Journal of Remote Sensing, 24(21), 4233–4240.

De Carvalho, O. A., Meneses, P. R. (2000). Spectral correlation mapper (SCM): An improvement on the spectral angle mapper (SAM). Summaries of the 9th JPL Airborne Earth Science Workshop.

El Hjouji, A. (1990). Etude des altérations du gisement aurifère de Tiouit (Saghro Oriental).

El Maghraoui, L., Popov, A. (1982). Les critères géologiques de la recherche des gisements subaffleurants d'or et d'argent (W, Cu, Mo), dans le Saghro oriental.

Gabr, S. S., Hassan, S. M., Sadek, M. F. (2015). Prospecting for new gold-bearing alteration zones at El-Hoteib area, South Eastern Desert, Egypt, using remote sensing data analysis. Ore Geology Reviews, 71, 1–13.

Gasquet, D. (1991). Genèse d'un pluton composite tardi-hercynien. Le massif du Tichka, Haut Atlas occidental (Maroc) [Thèse d'état]. Université Nancy I.

Gasquet, D., Ennih, N., Liégeois, J. P., Soulaimani, A., Michard, A. (2008). The Pan-African belt. In A. Michard, O. Saddiqi, A. Chalouan, D. Frizon de Lamotte (Eds.), Continental Evolution: The Geology of Morocco (Vol. 116, pp. 33–64). Springer-Verlag, Berlin Heidelberg.

Hassan, S. M., Sadek, M. F. (2017). Geological mapping and spectral based classification of basement rocks using remote sensing data analysis: The Korbiai-Gerf nappe complex, South Eastern Desert, Egypt. Journal of African Earth Sciences, 134, 404–418.

Hawkins, M. P., Beddoe-Stephens, B., Gillespie, M. R., Loughlin, S., Barron, H. F., Barnes, R. P., Powell, J. H., Waters, C. N., Williams, M. (2001). Carte géologique du Maroc au 1/50 000, feuille Tiouit (No. 404; Notes et Mémoires). Service Géologique du Maroc.

Hefferan, P. K., Karson, J. A., Saquaque, A. (1992). Proterozoic collisional basins in Pan-African suture zone, Anti-Atlas Mountains, Morocco. Precambrian Research, 54, 295–319.

Hunt, G. R. (1977). Spectral signatures of particulate minerals in the visible and near infrared. Geophysics, 42, 501–513.

Hunt, G. R., Ashley, P. (1979). Spectra of altered rocks in the visible and near infrared. Economic Geology, 74(7), 1613–1629.

Hunter, E. L., Power, C. H. (2002). An assessment of two classification methods for mapping Thames Estuary intertidal habitats using CASI data. International Journal of Remote Sensing, 23(15), 2989–3008.

Huntington, J. F. (2007). The Role of Remote Sensing in Finding Hydrothermal Mineral Deposits on Earth. In G. R. Bock J. A. Goode (Eds.), Ciba Foundation Symposium 202 - Evolution of Hydrothermal Ecosystems on Earth (And Mars?). https://doi.org/10.1002/9780470514986.ch12

Jettane, A. (1995). Le gisement d'or de Tiouit (Anti-Atlas Oriental, Maroc): Etudes des phases fluides et caractérisation des géothermes aurifères [Thèse d'état]. Université Mohammed V, École nationale de l'industrie minérale, Rabat, Maroc.

Kruse, F. A., Bordman, J. W., Huntington, J. F. (2003). Comparison of airborne hyperspectral data and EO-1 Hyperion for mineral mapping. IEEE Transactions on Geoscience and Remote Sensing, 41(6), 1388–1400.

Kruse, F. A., Lefkoff, A. B., Boardman, J. W., Heidebrecht, K. B., Shapiro, A. T., Barloon, P. J., Goetz, A. F. H. (1993). The spectral image processing system (SIPS)—Interactive visualization and analysis of imaging spectrometer data. Remote Sensing of Environment, 44(2–3), 145–163.

Leblanc, M., Lancelot, J. (1980). Interprétation géodynamique du domaine panafricain (Précambrien terminal) de l'Anti-Atlas (Maroc) à partir de données géologiques et géochronologiques. Canadian Journal of Earth Sciences, 17(1), 142–155.

Liu, J. G., Mason, P. J. (2016). Image processing and GIS for remote sensing: Techniques and applications. John Wiley and Sons.

Mathieux, P., Loredo Peretz, J., Argollo, J. (1982). Etude minéralogique et pétrographique de la mine de Tiouit.

Miftah, A., El Azzab, D., Attou, A., Ouchchen, M., Mamouch, Y., Achkouch, L., Soulaimani, A., Soulaimani, S., Manar, A. (2022). Mapping of favourable mining areas in the Tiouit area by multispectral remote sensing and airborne gamma-ray spectrometry coupled with geochemical data (Eastern Anti-Atlas, Morocco). Applied Earth Science, 131(3), 149_166. https://doi.org/10.1080/25726838.2022.2089967

Rowan, L. C., Mars, J. C. (2003). Lithologic mapping in the Mountain Pass, California area using Advanced Spaceborne Thermal Emission and Reflection Radiometer (ASTER) data. Remote Sensing of Environment, 84(3), 350–366.

Sabins, F. F. (1999). Remote sensing for mineral exploration. Ore Geology Reviews, 14, 157–183.

Saquaque, A. (1992). Un exemple de suture-arc: Le Précambrien de l'Anti-Atlas centre-oriental [PhD Thesis]. Université Cadi Ayyad, Marrakech.

Schwarz, J., Staenz, K. (2001). Adaptive threshold for spectral matching of hyperspectral data. Canadian Journal of Remote Sensing, 27(3), 216–224.

Van der Meer, F., Vazquez-Torres, M., Van Dijk, P. M. (1997). Spectral characterization of ophiolite lithologies in the Troodos Ophiolite complex of Cyprus and its potential in prospecting for massive sulphide deposits. International Journal of Remote Sensing, 18(6), 1245–1257.

Yuhas, R. H., Goetz, A. F., Boardman, J. W. (1992). Discrimination among semi-arid landscape endmembers using the spectral angle mapper (SAM) algorithm. https://ntrs.nasa.gov/archive/nasa/casi.ntrs.nasa.gov/19940012238.pdf

Zoheir, B., Emam, A. (2014). Field and ASTER imagery data for the setting of gold mineralization in Western Allaqi–Heiani belt, Egypt: A case study from the Haimur deposit. Journal of African Earth Sciences, 99, 150–164.